Soft Route to 4D Tomography

Thibault Taillandier-Thomas,* Stéphane Roux,† and François Hild‡
Laboratoire de Mécanique et Technologie, ENS Cachan/CNRS-UMR 8535/Univ. Paris-Saclay, 61 Avenue du Président Wilson, 94235 Cachan cedex, France
(Received 3 September 2015; published 6 July 2016)

Based on the assumption that the time evolution of a sample observed by computed tomography requires many less parameters than the definition of the microstructure itself, it is proposed to reconstruct these changes based on the initial state (using computed tomography) and very few radiographs acquired at fixed intervals of time. This Letter presents a proof of concept that for a fatigue cracked sample its kinematics can be tracked from no more than two radiographs in situations where a complete 3D view would require several hundreds of radiographs. This 2 order of magnitude gain opens the way to a "computed" 4D tomography, which complements the recent progress achieved in fast or ultrafast computed tomography, which is based on beam brightness, detector sensitivity, and signal acquisition technologies.

DOI: 10.1103/PhysRevLett.117.025501

Away from medical and biological applications [1], 3D imaging has revolutionized materials science [2–4]. From imaging aiming at visualization to a more quantitative assessment of material morphology, from synchrotron facilities to lab-scale equipment, from several-hour scans to ultrafast acquisitions lasting no more than a fraction of a second, x-ray computed tomography is becoming an easily accessible, user-friendly, high-performance technique. For applications such as metrology and nondestructive testing, it is also becoming much more common in industry.

In recent years, one striking trend is the recourse to 4D imaging to track in time the microstructure of a sample [4–6]. The fantastic achievements (e.g., tomography of metal solidification [5] or even of live flying insects [7]) have been made possible only through the development of fast data acquisition techniques.

4D imaging comes with a huge data flow that suggests to follow similar approaches as those developed for movies. Storing every single time frame on its own is highly redundant. The $(t+1)$ frame is usually very close to the (t) frame, and, hence, storing the complete (t) frame and the "sparse" difference between times $(t+1)$ and (t) requires much less data than both images independently, as evidenced in movie compression standards [8]. Based on a similar observation, Ref. [9] recently proposed denoising strategies with subset-based restoration techniques in 3D plus time in order to compensate for the missing information due to fewer projections. The efficiency of movie compression lies in the "sparsity" of the difference (especially when motion is accounted for) that has to be described in a suited language. Pushing the analogy into the field of tomography suggests that after the full 3D state of a sample in its initial state has been acquired, it is possible to reconstruct only the differences between two consecutive 3D images from many less projections. The present Letter aims to explore this route, whereby an enhanced 4D rate would be obtained *algorithmically* through a specific reconstruction rather than from the acquisition equipment. Only a single time step is considered in the present Letter while further indications for 4D tomography are given in the Supplemental Material [10]. In practice, both software and hardware strategies should be combined rather than opposed to reach extreme time resolutions.

Tomography consists of computing the 3D image $f(\boldsymbol{x})$, such that for a large set of directions θ, the projection (i.e., the integral of the x-ray absorption coefficient) matches the acquired projection $p(\boldsymbol{r},\theta)$ (i.e., the cologarithm of the beam intensity acquired at pixel $\boldsymbol{r}$ on the detector, normalized by the beam intensity at the same detector position without a sample)

$$\Pi_\theta f(\boldsymbol{x}) = p(\boldsymbol{r},\theta), \tag{1}$$

where Π_θ is the projection operator.

Mathematically, the reconstruction problem corresponds to a Radon transform relating the 3D image $f(\boldsymbol{x})$ to $p(\boldsymbol{r},\theta)$ that is to be inverted. Solving for $f(\boldsymbol{x})$ from $p(\boldsymbol{r},\theta)$ is a well-mastered problem for which different algorithms are known with their respective merits [14]. In discrete form, the sampling in angle θ should be chosen such that the maximum displacement of a voxel in $f(\boldsymbol{x})$ between two consecutive angular positions should be smaller than a detector pixel size, thus, leading to a number of angles proportional to the diameter of the sample (measured in detector pixels). Hence, a tomographic image whose cross section is $N_x \times N_x$ pixels with, e.g., $N_x = 1000$, requires usually about $N_\theta \approx 1600$ projections. Algebraic reconstruction techniques can help reduce N_θ, although it cannot be less than N_x without further assumptions on the image texture.

As a side remark, let us note that prescribing further constraints on the to-be-reconstructed image, such as the

discreteness of gray levels [15] down to binary images [16,17], sparse nonzero pixels [18], or a sparse boundary between constant value domains [19], may constitute a very efficient way of reducing the number of needed projections, compensating for a lack of projection data with specific *a priori* assumptions. In contrast, the present Letter aims to address arbitrary images.

Many different scenarios may be considered for describing the time evolution of a studied sample, a generic category of which is *motion*, including deformation. One classical tool used to quantitatively study such an evolution is digital volume correlation (DVC) [20,21], an extension to 3D images of digital image correlation [22]. This technique consists of registering two 3D images acquired (or reconstructed) at different times, t_0 and t_1, by accounting for a displacement field $\boldsymbol{u}(\boldsymbol{x}; t_1, t_0)$. Assuming the image texture has only been subjected to a geometrical transformation, the following DVC functional operating on an arbitrary displacement field $\boldsymbol{v}(\boldsymbol{x})$ is introduced

$$\mathcal{T}_{\mathrm{DVC}}[\boldsymbol{v}] = \int [f(\boldsymbol{x}, t_0) - f(\boldsymbol{x} + \boldsymbol{v}(\boldsymbol{x}), t_1)]^2 d\boldsymbol{x}. \quad (2)$$

Global DVC [23] further constrains the displacement field to be a linear combination of a chosen set of fields $\boldsymbol{\varphi}_i(\boldsymbol{x})$ for $i = 1, \ldots, N_v$,

$$\boldsymbol{v}(\boldsymbol{x}) = \sum_i v_i \boldsymbol{\varphi}_i(\boldsymbol{x}). \quad (3)$$

A general example of kinematic bases well suited to mechanical modeling is those used in the framework of the finite element method. A mesh supporting finite element shape functions can be used, thereby ensuring displacement continuity (higher regularity can be chosen according to the shape function order). Finally, the displacement field is obtained from the minimization of the above functional [22]

$$\boldsymbol{u}_{\mathrm{DVC}}(\boldsymbol{x}; t_1, t_0) = \mathrm{Argmin}_{\boldsymbol{v}}(\mathcal{T}_{\mathrm{DVC}}[\boldsymbol{v}]) \quad (4)$$

with respect to vector $\boldsymbol{v}$ gathering all unknown amplitudes v_i. Let us stress that the number of parameters N_v needed to describe the kinematics is *always* much lower than the number of voxels in the 3D images, opening the way to reducing the number of projections.

Because the reference state is typically the rest state, time is available for carrying out a complete 3D image at time t_0 using as many projections as needed to obtain $f(\boldsymbol{x}, t_0)$. For later times, only a few projections are assumed to be available, which would not be sufficient to reconstruct the corresponding 3D volume. For any displacement field $\boldsymbol{v}(\boldsymbol{x})$, the full 3D image $f(\boldsymbol{x}, t_0)$ is advected to a deformed state that should be compared with known projections. Registration is now evaluated from the projection-based residuals only

$$\mathcal{T}_{\text{P-DVC}}[\boldsymbol{v}] = \int \{\Pi_\theta f[\boldsymbol{x} - \boldsymbol{v}(\boldsymbol{x}), t_0] - p(\boldsymbol{r}, \theta, t_1)\}^2 d\boldsymbol{x}, \quad (5)$$

and the Eulerian displacement field is the minimizer of this functional

$$\boldsymbol{u}_{\text{P-DVC}} = \mathrm{Argmin}_{\boldsymbol{v}}(\mathcal{T}_{\text{P-DVC}}[\boldsymbol{v}]). \quad (6)$$

Because an accurate computation of the projected deformed volume is needed, this approach is not easily extendable to "local tomography".

Such an approach (referred to as P-DVC in the following) was originally proposed in Ref. [24] and tested on a simple geometry where the strain magnitude was very small so that a rigid body motion revealed to be a fair approximation. It was observed that although the basic principles of the methodology were sound, the uncertainty of the measured displacement field was larger along the boundaries of the solid because the mesh had to strictly enclose the actual sample and because at the boundaries, the phase contrast effects are present although neglected in the reconstruction. Moreover, it was also noticed that fine meshes led to numerical instabilities due to ill-conditioning. Thus, it is legitimate to ask whether the method would resist a much more difficult test involving a complex kinematics and requiring a fine mesh.

To make the problem well-posed, the effective number of degrees of freedom has to be reduced, yet it is important to be able to deal with a fine mesh to precisely account for the sample geometry and kinematics. One way to satisfy these two opposite requirements is to consider soft Tikhonov regularization [25]. This implies a penalty to be added to the functional $\mathcal{T}_{\mathrm{DVC}}$ as the displacement field departs from an expected property. Classically, terms like the amplitude of the displacement $\|\boldsymbol{u}\|$ or of the norm of its gradient are used, although they introduce unphysical bias. It is preferred to introduce a penalty to deviations from the solution to a homogeneous elastic problem [11,26,27]. Introducing the (infinitesimal) strain tensor $\boldsymbol{\varepsilon} = (1/2)[\boldsymbol{\nabla u} + (\boldsymbol{\nabla u})^t]$, Hooke's tensor $\mathbf{C}$ that relates stress $\boldsymbol{\sigma}$ and strain $\boldsymbol{\sigma} = \mathbf{C} : \boldsymbol{\varepsilon}$, the balance equation in the absence of body forces $\boldsymbol{\nabla} \cdot \boldsymbol{\sigma} = \mathbf{0}$ shows that the elastic displacement field obeys the second order homogeneous differential equation $\boldsymbol{\nabla} \cdot \mathbf{C} : \boldsymbol{\nabla v} = \mathbf{0}$. The choice is made to introduce a penalty on the quadratic norm of the left member of this equation referred to as the *equilibrium gap*, which reads

$$\mathcal{T}_{\mathrm{reg}}[\boldsymbol{v}] = \int \|\boldsymbol{\nabla} \cdot C : \boldsymbol{\nabla v}\|^2 d\boldsymbol{x}. \quad (7)$$

Adding the two contributions $\mathcal{T}_{\text{P-DVC}}$ and $\mathcal{T}_{\mathrm{reg}}$ naturally selects a length scale. To make it more explicit and, hence, easy to tune, a specific displacement orientation $\boldsymbol{w}_0$ and wave vector $\boldsymbol{k}_0$ are chosen. Based on the trial displacement field $\boldsymbol{v}_0(\boldsymbol{x}) = \boldsymbol{w}_0 \exp(i\boldsymbol{k}_0 \cdot \boldsymbol{x})$, the total functional is written as

$$\mathcal{T}_{\text{tot}}[\boldsymbol{v}] = \frac{\mathcal{T}_{\text{P-DVC}}[\boldsymbol{v}]}{\mathcal{T}_{\text{P-DVC}}[\boldsymbol{v}_0]} + (|\boldsymbol{k}_0|\xi)^4 \frac{\mathcal{T}_{\text{reg}}[\boldsymbol{v}]}{\mathcal{T}_{\text{reg}}[\boldsymbol{v}_0]}. \quad (8)$$

The meaning of regularization length ξ stems from the above expression. Namely, at long wavelengths, $\mathcal{T}_{\text{P-DVC}}$ is dominant, and, hence, image registration determines the displacement, whereas at short wavelengths, the regularization length produces a smooth and differentiable displacement field. If a large ξ is not faithful to reality then the residuals will display a large value, motivating for lowering ξ down to values such that the residuals are comparable with the residual level observed for the reference image where the displacement is null. A much more extensive discussion on regularization is provided in the Supplemental Material [10].

Let us stress that the above regularization does not require the specimen to strictly obey linear elasticity. Rather, it may be seen as a filter that dampens abrupt displacement gradients with reference *locally* to the solution to an elastic problem. Let us note that a viscous fluid, a viscoelastic solid, or a material exhibiting plasticity, viscoplasticity, or a damage behavior would all locally display an incremental relationship between strain and stress rates that has the same algebraic form as that of an elastic problem, with the difference of being spatially heterogeneous. Therefore, at the expense of being locally less precise than using a complete mechanical modeling, the above filter appears to be very generic. It is to be noted that the limit of an infinite regularization length ξ is well defined; namely, the problem consists of solving for the minimization of $\mathcal{T}_{\text{P-DVC}}[\boldsymbol{v}]$, Eq. (5), for $\boldsymbol{v}$ in the regularization kernel, $\mathcal{T}_{\text{reg}}[\boldsymbol{v}] = 0$. The elastic problem itself is well-posed once the boundary conditions are set, and, hence, the problem reduces precisely to the determination of the boundary conditions. The regularization length ξ can also be tuned down to small values comparable to the element size so that regularization is essentially deactivated. In the first limit, the number of effective degrees of freedom is that accounting for the boundary conditions (i.e., nodes on the surfaces where displacement is to be set), whereas in the second one, all nodes of the mesh have an unknown displacement vector. The limitation of the latter case is that the conditioning of the problem will get poorer as ξ decreases, and a possible remedy would imply an increase of the number of needed projections. Yet, for a very small size such as $\xi = 10$ voxels, the number of effective independent degrees of freedom is of the order of 300 times less than the number of voxels, thus, potentially leading to more than 2 orders of magnitude gain in the number of projections. The effect of tuning the regularization length is illustrated in the Supplemental Material [10].

The following example describes the application of the proposed strategy to a *real test case* in order to demonstrate that the above strategy works with no more than two projections and this for a specimen containing a crack where a very fine mesh is to be utilized.

A cast iron sample containing well-dispersed 50-μm nodular graphite particles was subjected to cyclic loading so that a fatigue crack propagated throughout a large portion of the cross section. The test was performed *in situ* at the European Synchrotron Radiation Facility (ID19 beam line, 60-keV energy) so that a series of tomographic images could be acquired at different stages of loading and/or crack growth.

The region of interest size is $1.67 \times 1.72 \times 2.59$ mm^3 or $330 \times 340 \times 512$ voxels, with a voxel size chosen to be 5.06 μm. A full reconstruction requires $N_\theta = 600$ projections. Several volumes were imaged at different load levels (50, 100, and 140 N). In the following, the selected pair of states is chosen after 30 000 cycles (close to failure that occurred after 50 000 cycles). The reference state is chosen at a small but nonzero tensile load of 12 N to cancel out possible plays of the tensile stage. The deformed state was that obtained for the highest load level (i.e., 140 N) for the test to be discriminating.

The trace of the crack was visible on the reference state of the sample, and, hence, it was possible to segment the crack and produce a fine mesh where the two crack faces were separated. Figure 1 shows the mesh superimposed onto the microstructure. It consists of four-noded tetrahedron (i.e., T4) elements with about 2100 nodes and 8500 T4 elements. At the crack tip, the mesh was refined with element sizes down to 15 voxels. Alternatively, an eXtended Finite Element Method [12] strategy could have been used.

The minimization of the total functional based on projections is considered. The limit of the regularization length ξ tending to infinity is selected so that the only

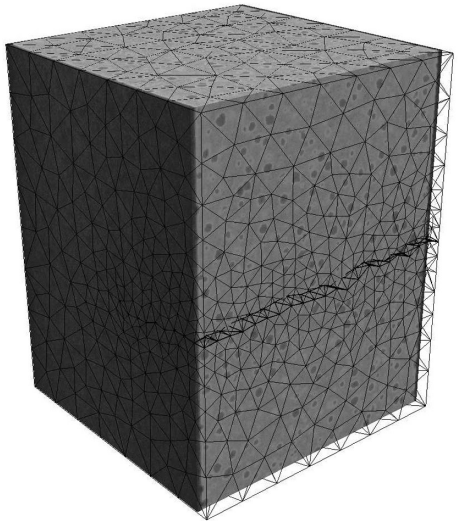

FIG. 1. Nodular graphite cast iron sample and superimposed fine mesh. The sample is in its reference state for a 12-N tensile load.

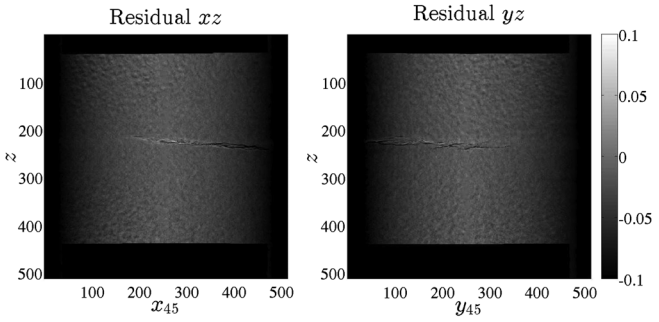

FIG. 2. Difference between actual projections of the deformed state and projections of the corrected reference volume. The left and right views are the two projections that are used for P-DVC.

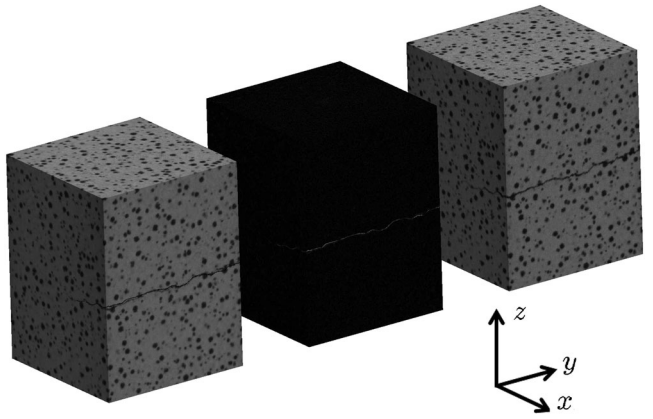

FIG. 3. (Left) Advected reference volume using the P-DVC estimated displacement field. (Right) Reconstructed deformed volume. (Center) Absolute difference between the two preceding volumes.

unknowns are the boundary conditions along the top and bottom faces. The latter sections are moreover considered as rigid so that only 12 unknowns remain to be determined. The number of projection directions (chosen to be perpendicular) that are considered is $N_\theta = 2$. Let us stress that imaging the entire volume required more than 2 orders of magnitude more numerous radiographs, $N_\theta = 600$.

The determination of the displacement field was obtained from the minimization of the functional $\mathcal{T}_{\text{tot}}$ using a Gauss-Newton procedure. Convergence was observed to be reached within about five iterations only.

One way to evaluate the quality of the procedure is to consider the difference between the two projection images whose quadratic norm is the integrand of Eq. (5). These differences called "projection residuals" are shown in Fig. 2. Qualitatively, it is observed that most features of the projections have disappeared in the residuals, but the projection of the crack whose morphology is only approximately captured by the mesh and where phase contrast effects—not modeled in the procedure—are expected. Quantitatively, the gauge to interpret faithfully the level of residuals is provided by applying the P-DVC procedure to a deformed state that is chosen as the reference. The displacement is identically null, yet the projection of the reconstruction in the two chosen directions is never exactly equal to the recorded projections because of acquisition imperfections as well as reconstruction or projection biases. These baseline residual levels amount to a signal-to-noise ratio (SNR) of about 31.5 dB for the projections. The same estimate for the actual deformed sample leads to a SNR $\approx$ 30 dB, which is only about 1.5 dB lower. Hence, reconstruction, projection, and interpolation are responsible for most of the remaining residuals, thereby validating the registration process.

The initial claim was that the proposed technique would allow us to track the entire 3D volume although only two projections were used. In the discussed example, the entire set of 600 projections had been acquired so that one may directly compare the reference volume advected by the estimated P-DVC displacement field and the direct reconstruction of the deformed volume. These two volumes and their difference are shown in Fig. 3. The difference between the volumes reveals mostly reconstruction artifacts that impact differently the two procedures and slight inaccuracies in the description of the crack geometry from segmentation and meshing. The SNR estimated on the reconstructed volume amounts to 24 dB, to be compared to 25 dB when the displacement field issued from standard DVC (based on volumes), and 30 dB when the proposed P-DVC is applied to the reference volume itself, and the displacement field (that should ideally be 0) is used to "correct" the volume. Similarly, the rms difference between displacement fields obtained from P-DVC and standard DVC amounts to 0.18 voxel. The Supplemental Material [10] presents additional details on the influence of the chosen reconstruction procedure, mesh fineness, or regularization length for this experimental example.

It has been shown that considering (even complex) kinematics regularized through an equilibrium-gap elastic penalization as a regularization allowed for tracking the time evolution of a loaded cracked sample. In this experimental test case, the number of projections was reduced from 600 down to 2. The low level of residuals and the very good agreement with standard DVC constitute a validation of the proposed principle.

The presented analysis is based on the assumption that the temporal evolution of the specimen is due to motion and that this motion can be (at least at small scales) approached by an elastic problem. Cases where the microstructure topology changes—as when a new phase appears (e.g., void nucleation), when two features merge into one (coalescence), or when an unexpected crack initiates—fall out of the scope of the proposed formalism. However, it is believed that the general philosophy remains valid. Namely, provided the evolution can be modeled faithfully with a number parameters that is much smaller than the voxel number, then matching virtual (computed) projections with a set of few actual projection allows us to track

the time evolution with few radiographs and, hence, at a high rate. This methodology opens the way to an enhanced temporal resolution, i.e., 4D tomography, based on a data processing approach and no change in the required equipment.

The support of the ANR (the "ANR-11-BS09-027 EDDAM" project and the "Investissements d'Avenir" program under the reference "ANR-10-EQPX-37 MATMECA") is gratefully acknowledged. The tomographic data used in this Letter have been obtained at the European Synchrotron Radiation Facility on beam line ID19 during experiment MA-501 and benefitted from the framework of the Long Term Project No. HD501. The authors acknowledge the precious help of C. Jailin for significantly improving the quality of reconstruction thanks to a specific flat-field correction procedure. Reconstruction benefitted from the reconstruction software ASTRA [13].

*thibault.taillandier-thomas@lmt.ens-cachan.fr
†stephane.roux@lmt.ens-cachan.fr
‡francois.hild@lmt.ens-cachan.fr

[1] K. Doi, Current status and future potential of computer-aided diagnosis in medical imaging, Br. J. Radiol. **78**, S3 (2005).
[2] E. Maire, J.-Y. Buffière, L. Salvo, J.-J. Blandin, W. Ludwig, and J. M. Letang, On the application of X-ray microtomography in the field of materials science, Adv. Eng. Mater. **3**, 539 (2001).
[3] J. Baruchel, J.-Y. Buffiere, P. Cloetens, M. Di Michiel, E. Ferrie, W. Ludwig, E. Maire, and Luc Salvo, Advances in synchrotron radiation microtomography, Scr. Mater. **55**, 41 (2006).
[4] E. Maire and P. J. Withers, Quantitative X-ray tomography, Int. Mater. Rev. **59**, 1 (2014).
[5] L. Salvo, M. Di Michiel, M. Scheel, P. Lhuissier, B. Mireux, and M. Suéry, Ultra fast in situ x-ray micro-tomography: Application to solidification of aluminium alloys, Mater. Sci. Forum **706**, 1713 (2012).
[6] A. Ulvestad, A. Tripathi, S. O. Hruszkewycz, W. Cha, S. M. Wild, G. B. Stephenson, and P. H. Fuoss, Coherent diffractive imaging of time-evolving samples with improved temporal resolution, Phys. Rev. B **93**, 184105 (2016).
[7] S. M. Walker, D. A. Schwyn, R. Mokso, M. Wicklein, T. Müller, M. Doube, M. Stampanoni, H. G. Krapp, and G. K. Taylor, In vivo time-resolved microtomography reveals the mechanics of the blowy flight motor, PLoS Biol. **12**, e1001823 (2014).
[8] I. E. G. Richardson, *H.264 and MPEG-4 Video Compression: Video Coding for Next-Generation Multimedia* (John Wiley & Sons Ltd., Chichester, England, 2003).
[9] X. Jia, Y. Lou, B. Dong, Z. Tian, and S. Jiang, *Medical Image Computing and Computer-Assisted Intervention—MICCAI 2010* (Springer, Berlin, 2010), pp. 143–150.
[10] See Supplemental Material at http://link.aps.org/supplemental/10.1103/PhysRevLett.117.025501, which includes Refs. [11–13]. It provides additional information on elastic regularization, and its effect on inverse problems. It also details the case study of the main paper illustrating the effect of different elements of the data processing. Finally, it also discusses in more details practical implementation aiming to 4D tomography.
[11] T. Taillandier-Thomas, S. Roux, T. Morgeneyer, and F. Hild, Localized strain field measurement on laminography data with mechanical regularization, Nucl. Instrum. Methods Phys. Res., Sect. B **324**, 70 (2014).
[12] N. Sukumar, N. Moës, B. Moran, and T. Belytschko, Extended finite element method for three-dimensional crack modelling, Int. J. Numer. Methods Eng. **48**, 1549 (2000).
[13] W. van Aarle, W. J. Palenstijn, J. De Beenhouwer, T. Altantzis, S. Bals, K. J. Batenburg, and J. Sijbers, The ASTRA toolbox: A platform for advanced algorithm development in electron tomography, Ultramicroscopy **157**, 35 (2015).
[14] A. C. Kak and M. Slaney, *Principles of Computerized Tomographic Imaging* (Society for Industrial and Applied Mathematics, PA,USA, 2001).
[15] *Advances in Discrete Tomography and Its Applications*, edited by G. T. Herman and A. Kuba (Bikhäuser, Basel, 2007).
[16] K. J. Batenburg, A network flow algorithm for reconstructing binary images from discrete X-rays, J. Math. Imaging Vision **27**, 175 (2007); A network flow algorithm for reconstructing binary images from continuous X-rays, J. Math. Imaging Vision **30**, 231 (2008).
[17] E. Gouillart, F. Krzakala, M. Mezard, and L. Zdeborová, Belief-propagation reconstruction for discrete tomography, Inverse Probl. **29**, 035003 (2013).
[18] D. L. Donoho and J. Tanner, Precise undersampling theorems, Proc. IEEE **98**, 913 (2010).
[19] E. J. Candès, J. Romberg, and T. Tao, Robust uncertainty principles: exact signal reconstruction from highly incomplete frequency information, IEEE Trans. Inf. Theory **52**, 489 (2006).
[20] B. K. Bay, T. S. Smith, D. P. Fyhrie, and M. Saad, Digital volume correlation: Three-dimensional strain mapping using X-ray tomography, Exp. Mech. **39**, 217 (1999).
[21] M. Bornert and J. M. Chaix *et al.*, Mesure tridimensionnelle de champs cinématiques par imagerie volumique pour l'analyse des matériaux et des structures, Instrum. Mes. Métrol. **4**, 43 (2004).
[22] M. A. Sutton, J. J. Orteu, and H. Schreier, *Image Correlation for Shape, Motion and Deformation Measurements* (Springer Verlag-US, New York, 2009).
[23] S. Roux, F. Hild, P. Viot, and D. Bernard, Three-dimensional image correlation from X-ray computed tomography of solid foam, Comp. Part A **39**, 1253 (2008).
[24] H. Leclerc, S. Roux, and F. Hild, Projection savings in CT-based digital volume correlation, Exp. Mech. **55**, 275 (2015).
[25] A. N. Tikhonov and V. Y. Arsenin, *Solutions of Ill-Posed Problems* (Winston, Washington, DC, 1977).
[26] J. Réthoré, S. Roux, and F. Hild, An extended and integrated digital image correlation technique applied to the analysis fractured samples; The equilibrium gap method as a mechanical filter, Eur. J. Comput. Mech. **18**, 285 (2009).
[27] H. Leclerc, J. N. Périé, F. Hild, and S. Roux, Digital volume correlation: What are the limits to the spatial resolution?, Mech. Ind. **13**, 361 (2012).